

Stellar winds pump the heart of the Milky Way

DIEGO CALDERÓN,^{1,2,3} JORGE CUADRA,¹ MARC SCHARTMANN,^{4,5,2} ANDREAS BURKERT,^{5,2,4} AND CHRISTOPHER M. P. RUSSELL¹

¹*Instituto de Astrofísica, Facultad de Física, Pontificia Universidad Católica de Chile, 782-0436 Santiago, Chile*

²*Max Planck Institute for Extraterrestrial Physics, P.O. Box 1312, Giessenbachstr. 1, D-85741 Garching, Germany*

³*Institute of Theoretical Physics, Faculty of Mathematics and Physics, Charles University, 180 00 Prague, Czech Republic*

⁴*Excellence Cluster Origins, Ludwig-Maximilians-Universität München, Boltzmannstr. 2, D-85748 Garching, Germany*

⁵*Universitätssternwarte der Ludwig-Maximilians-Universität, Scheinerstr. 1, D-81679 München, Germany*

(Received December 5, 2019; Revised December 5, 2019; Accepted December 5, 2019)

Submitted to ApJ

ABSTRACT

The central super-massive black hole of the Milky Way, Sgr A*, accretes at a very low rate making it a very underluminous galactic nucleus. Despite the tens of Wolf-Rayet stars present within the inner parsec supplying $\sim 10^{-3} M_{\odot} \text{ yr}^{-1}$ in stellar winds, only a negligible fraction of this material ($< 10^{-4}$) ends up being accreted onto Sgr A*. The recent discovery of cold gas ($\sim 10^4$ K) in its vicinity raised questions about how such material could settle in the hostile ($\sim 10^7$ K) environment near Sgr A*. In this work we show that the system of mass-losing stars blowing winds can naturally account for both the hot, inefficient accretion flow, as well as the formation of a cold disk-like structure. We run hydrodynamical simulations using the grid-based code RAMSES starting as early in the past as possible to observe the state of the system at the present time. Our results show that the system reaches a quasi-steady state in about ~ 500 yr with material being captured at a rate of $\sim 10^{-6} M_{\odot} \text{ yr}^{-1}$ at scales of $\sim 10^{-4}$ pc, consistent with the observations and previous models. However, on longer timescales ($\gtrsim 3000$ yr) the material accumulates close to the black hole in the form of a disk. Considering the duration of the Wolf-Rayet phase ($\sim 10^5$ yr), we conclude that this scenario likely has already happened, and could be responsible for the more active past of Sgr A*, and/or its current outflow. We argue that the hypothesis of the mass-losing stars being the main regulator of the activity of the black hole deserves further consideration.

Keywords: Galaxy: center — hydrodynamics — stars: winds, outflows — accretion, accretion disks

1. INTRODUCTION

Murchikova et al. (2019) recently detected cold gas ($\sim 10^4$ K) at short distances ($\sim 10^{-3}$ pc) from the Milky Way central super-massive black hole (SMBH), Sgr A*. The observation of a relatively wide ($\sim 2200 \text{ km s}^{-1}$) double-peaked H30 α recombination line suggests the presence of a disk-like structure made out of such material. On the other hand, *Chandra* observations reveal that the innermost parsec of Sgr A* is filled with hot ($\sim 10^7$ K) and diffuse plasma with a mean density of $\sim 10 \text{ cm}^{-3}$ (Baganoff et al. 2003; Wang et al. 2013;

Russell et al. 2017). This material is constantly being supplied by the powerful outflows of the tens of Wolf-Rayet (WR) stars inhabiting the region at 1–10 arcsec from Sgr A* (Paumard et al. 2006; Yelda et al. 2014)¹. Additionally, the G2 object (Gillessen et al. 2012), as well as the bright knots in the IRS 13E cluster (Fritz et al. 2010), correspond to cold sources in this region that are observed in the Br- γ recombination line. How such cold gas structure could form in such a hot and hostile environment remains unexplained.

¹ Given the mass and distance of Sgr A* ($4.3 \times 10^6 M_{\odot}$ and 8.3 kpc), 1 arcsec $\approx 0.04 \text{ pc} \approx 10^5$ Schwarzschild radii.

In total, the mass flow rate supplied by the WR stars is estimated to be $\sim 10^{-3} M_{\odot} \text{ yr}^{-1}$ (Martins et al. 2007). However, the detection of polarised emission at sub-mm wavelengths has constrained the accretion rate at hundreds of Schwarzschild radii ($\sim 10^{-5} \text{ pc}$) to be many orders of magnitude smaller (10^{-9} – $10^{-7} M_{\odot} \text{ yr}^{-1}$; Marrone et al. 2006, 2007). Although this is a very low accretion rate, it could have been different in the past. Since the early 90s, many authors have argued that Sgr A* was more active in the past, specifically about hundreds of years ago (Sunyaev et al. 1993; Koyama et al. 1996; Ponti et al. 2010), and even as little as decades ago (Muno et al. 2007). Such hypotheses rely on X-ray light echoes observations of molecular clouds located at hundreds of parsecs from the SMBH. Based on long-exposure X-ray observations of the inner parsec, Wang et al. (2013) ruled out a Bondi (steady state inflow) solution for the plasma distribution in the region. Instead, the distribution showed agreement with an outflow solution, which supports the past activity hypothesis.

Numerical hydrodynamics models of the system of WR stars have been able to reproduce the mass inflow rate at the Bondi radius ($\sim 10^{-6} M_{\odot} \text{ yr}^{-1}$; Cuadra et al. 2008, 2015; Russell et al. 2017), and even deeper relatively well (Ressler et al. 2018). These studies simulated the system starting 1100 yr in the past and evolved it to reach a quasi-steady state at the present. Nevertheless, this timescale only manages to capture a single complete orbital period of the innermost WR star (see Figure 1). Furthermore, it is approximately two orders of magnitude smaller than the typical duration of the WR phase in massive stars of 10–25 M_{\odot} ($\sim 0.1 \text{ Myr}$; Crowther 2007). In reality, the WR stellar system will exist for even longer as the stars do not necessarily evolve coordinately in and off the WR phase. Thus, we should not draw strong conclusions of the long-term state of the system based on previous studies.

In this letter, we investigate, for the first time, the evolution of the system of mass-losing stars orbiting Sgr A* for longer timescales. Although we could not afford to simulate the system for timescales comparable to the typical duration of the WR phase ($\sim 0.1 \text{ Myr}$), we improve the simulation time of previous works by a factor \sim three. This work is presented as follows: Section 2 describes the numerical setup, initial conditions and assumptions. Section 3 presents the simulation and characterizes each phase of the evolution. Finally, in Section 4 we discuss implications and present the conclusions.

2. NUMERICAL SETUP

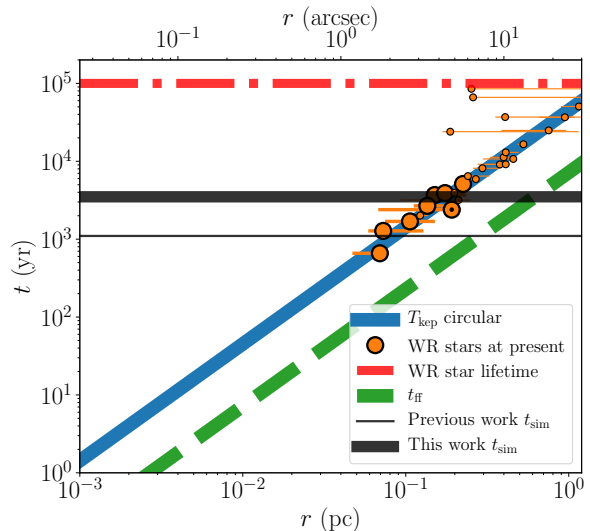


Figure 1. Timescales as a function of distance from Sgr A*. The solid blue line represents the circular Keplerian orbital period. The dashed green line shows the free-fall timescale. Orange circles denote the orbital periods of individual WR stars, with the horizontal orange segments indicating the separation change to Sgr A* due to their orbital eccentricity. Smaller symbols represent stars for which the eccentricities have been minimised when setting up their orbits (see Section 2). The circle with a black dot in its centre represents the star IRS 33E. The horizontal dash-dotted red line marks the WR phase duration. The horizontal solid thin and thick black lines indicate the simulation time of previous and current studies, respectively.

We developed 3D hydrodynamics simulations making use of the adaptive-mesh refinement (AMR) grid-based code RAMSES (Teyssier 2002). The code uses a second-order Godunov method to solve the equations of hydrodynamics. We consider an adiabatic equation of state, plus optically thin radiative cooling with $Z = 3Z_{\odot}$, where Z_{\odot} is the Solar mass fraction in metals (see Calderón et al. 2019, for a discussion). We use an exact Riemann solver together with a MonCen slope limiter (e.g., Toro 2009). The simulation setup considers the system of WR stars blowing stellar winds into the medium while they move under the influence of the gravitational potential of Sgr A* whose mass is $4.3 \times 10^6 M_{\odot}$ (Gillessen et al. 2017). For simplicity, we assume that the motion of the stars is completely determined by the gravity of the SMBH. The stars describe Keplerian orbits, which have been constrained through decade-long observational monitoring (Paumard et al. 2006; Gillessen et al. 2017). For the stars whose orbits have not been completely determined, we used the most likely trajectories expected for the members of the “clockwise disk” (Beloborodov et al. 2006), while the rest were cal-

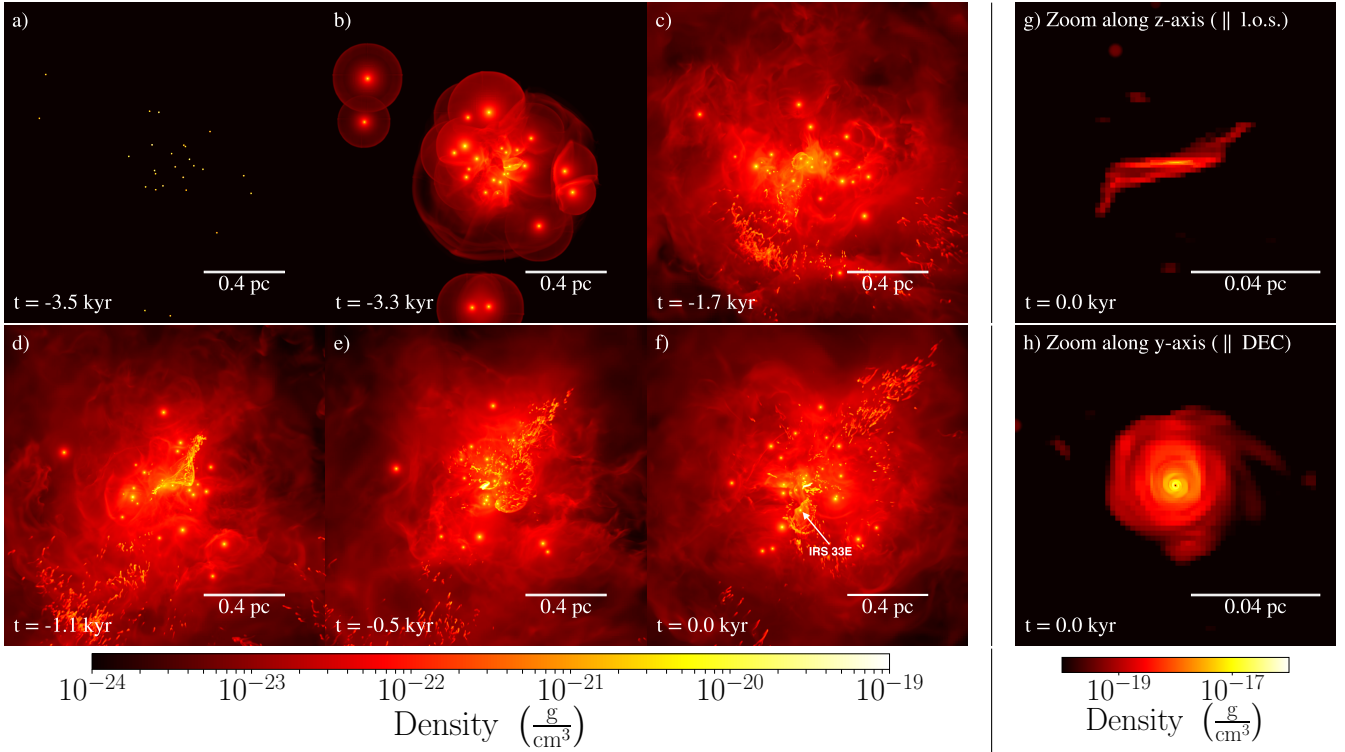


Figure 2. Complete evolution of the mass-losing stars orbiting Sgr A*. The panels a)-f) show projected density maps along the z -axis (parallel to the line-of-sight) weighted by density. The horizontal and vertical axes are parallel to right ascension and declination, respectively. Each panel shows the complete simulation domain at different simulation times. Panels g) and f) are zoomed density projection maps at $t = 0$ along the z - and y -axes, respectively, showing the disk-like structure around Sgr A*. Notice the change in the scale of the colorbar.

culated through minimizing their eccentricity (Cuadra et al. 2008). The stellar wind generation is simulated following the approach of Lemaster et al. (2007), and also used in Calderón et al. (2019). The properties of the stellar winds were taken from spectroscopic studies (Martins et al. 2007; Cuadra et al. 2008). In order to avoid artificial accumulation of material close to the black hole we set an open boundary of radius $2\sqrt{3}\Delta x$, where Δx is the size of the smallest cell. This sphere in the domain is reset after each time step to low density at rest and low pressure (Ressler et al 2018). The domain of the simulation is a cubic box of side length 1.6 pc (~ 40 arcsec) with outflow boundary conditions (zero gradients). The coarse resolution corresponds to 64^3 cells, plus four extra refinement levels ($\Delta x \approx 1.6 \times 10^{-3}$ pc). Instead, the stellar wind generation regions allow five extra refinement levels ($\Delta x \approx 7.8 \times 10^{-4}$ pc), while the vicinity of the inner boundary allows eight extra refinement levels ($\Delta x \approx 9.8 \times 10^{-5}$ pc). The initial position and velocity of the WR stars are determined extrapolating the state vectors to the past, so that the simulation evolves the system up to the present epoch (Cuadra et al. 2008, 2015; Ressler et al 2018). Most stars have periods of the order of $\sim 10^4$ yr and orbit around Sgr A* at a distance

of ~ 0.3 pc (see Figure 1). Although at such distances the free-fall timescale (dashed green line) is of the order of hundreds of year, it is not easy for the stellar wind material to shed its angular momentum, so it corresponds to a lower limit of the actual infalling timescale.

In this work, the simulation starts from 3500 yr in the past in order to study whether it is possible for the system to reach, and maintain steady state or not². As a control sample we run a model starting 1100 yr in the past, similar to previous works in the literature (Cuadra et al. 2008, 2015; Ressler et al 2018). The domain is initialized at very low density $\rho_{\text{ISM}} = 10^{-24}$ g cm $^{-3}$ at rest $\mathbf{u} = \mathbf{0}$, and low pressure $P_{\text{ISM}} = \rho_{\text{ISM}} c_{s,f}^2 \gamma^{-1}$, where $c_{s,f} = 10$ km s $^{-1}$ is the sound speed of the temperature floor ($T \approx 10^4$ K), and γ is the adiabatic index which is set to 5/3 for an adiabatic gas. This latter value was chosen, assuming that the strong ultraviolet radiation field of the young massive stars keeps the environment at such temperature.

² Ideally, we would like to start the simulation as early as possible but this incurs a very high computational cost: 3500 yr equates to $\sim 100,000$ cpu hours.

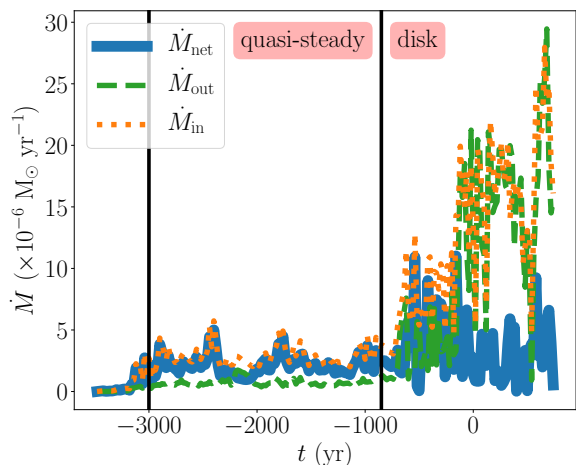


Figure 3. Mass flow rate across a sphere of radius 5×10^{-4} pc (1.25×10^{-2} arcsec). The absolute value of the net mass flow rate is shown by the solid blue line. The mass inflow and outflow rates are represented by the dotted orange and dashed green lines, respectively. The vertical solid black lines (at $t \approx -3000$ yr and $t \approx -800$ yr) divide the evolution into the transient, quasi-steady, and disk phases.

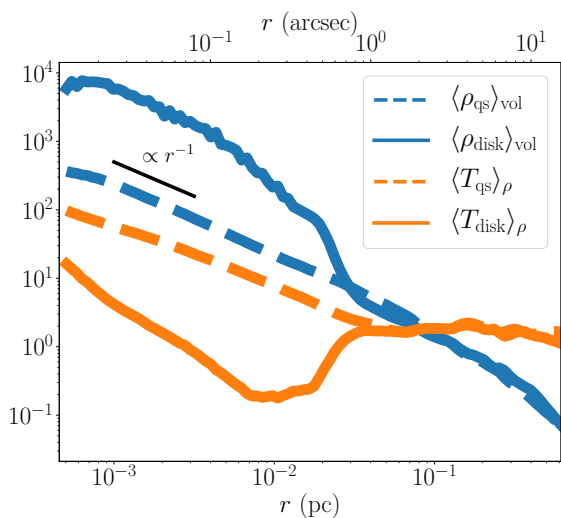


Figure 4. Density (blue lines) and temperature (orange lines) radial profiles in units of 10^{-22} g cm^{-3} and 10^7 K, respectively. The subscripts “qs” and “disk” refer to time-averaged quantities during the quasi-steady state (dashed lines) and the disk phase (solid lines), respectively.

3. HYDRODYNAMICS: EVOLUTION PHASES

Figure 2 shows density maps illustrating the time evolution of the simulation. Each map corresponds to a density projection of the full domain along the z -axis, which is parallel to the line-of-sight, weighted by den-

sity (i.e., $\int \rho^2 dz / \int \rho dz$)³. The horizontal and vertical axes are parallel to right ascension and declination, respectively. Panel a) shows the initial condition of the simulation at $t = -3500$ yr. Once the simulation starts, each star blows a wind, which develops a shock that at some point ends up colliding with the others (panel b). Such collisions create dense ($\sim 10^{-22}$ g cm^{-3}), hot material ($\sim 10^7$ K) that fills the entire domain relatively quickly (~ 500 yr). Notice how complex structures develop in the gas, e.g., the interaction of stellar winds, instabilities, dense clumps, and bow shocks forming due to the motion of the stars through the medium. This depends on cooling being efficient, which is sensitive to the stellar wind abundances. Fortunately, such abundances have been constrained through spectroscopic studies relatively well (see Calderón et al. 2019, for a more detailed justification). In panel c) the system has already attained what appears to be a quasi-steady state like in previous works in which the simulations end after a time comparable to the evolution time of panel d) (Cuadra et al. 2008; Ressler et al 2018). However, in panel g) it is possible to observe an accumulation of material at the center of the domain. Visually, this material seems to settle into a disk-like structure around Sgr A*, which is confirmed analyzing the central region in detail (see panels g and h). This material seems to mainly arise from the strong bow shock generated by the star IRS 33E traveling through the dense medium (panels d-f). Based on the appearance of the system we divide its evolution in three phases: the transient, quasi-steady, and disk phases.

Figure 3 shows the mass flow rate across a sphere of radius $\sim 5 \times 10^{-4}$ pc (1.25×10^{-2} arcsec) as a function of time, highlighting the transition between phases. This length scale is about two orders of magnitude smaller than the radius of the disk. In the transient phase the mass inflow rate increases up to $\sim 10^{-6}$ M_{\odot} yr^{-1} roughly at $t \approx -3000$ yr. Then, in the quasi-steady phase the net mass flow rate \dot{M}_{net} is variable but permanently inflowing and around the same order of magnitude. At $t \approx -800$ yr the system enters into the disk phase, whereby the formation and presence of the disk produces significant changes in both the inflow and outflow mass flow rates. In general, the net flow remains variable, but now its amplitude is about one order of magnitude larger due to the enhancement of the inflow and outflow rates. Notice that this behavior is observed even at $t > 0$.

³ This quantity helps to highlight the dense gas, which corresponds to the cold material which is most likely to contribute to the disk formation and the most refined regions of the domain.

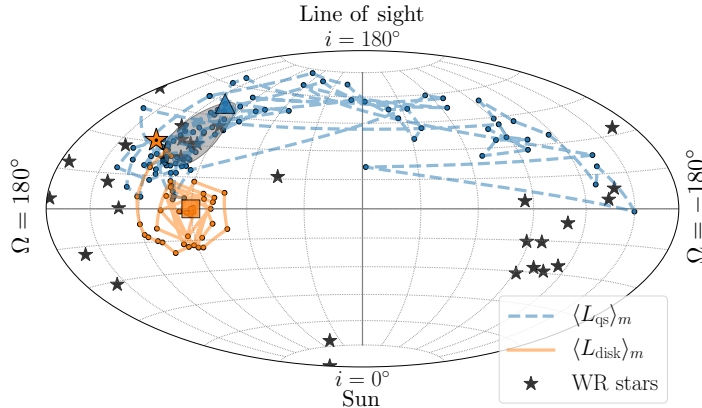


Figure 5. Orientation of the angular momentum of the gas enclosed in a sphere of radius 0.01 pc (0.25 arcsec), and the WR stars⁷. The vertical dimension represents inclination i , while the horizontal dimensions stand for the longitude of the ascending node Ω . Thus, a face-on star orbiting clockwise on the sky would be at the north pole of the graph. The dashed blue and solid orange lines represent the quasi-steady and disk phases, respectively. Each dot corresponds to the analysis of a single snapshot. The triangle and square show the initial and final state, respectively. The black stars represent the angular momentum direction of the WR stars, highlighting IRS 33E as an orange star with a black dot, instead. The grey shaded region corresponds to the direction of the clockwise disk at $(104^\circ, 126^\circ)$ with a thickness of 16° (Yelda et al. 2014).

Figure 4 shows the time-averaged density (blue lines) and temperature (orange lines) radial profiles. The averages were calculated over the quasi-steady (dashed lines) and the disk (solid lines) phases. Notice that in the quasi-steady phase both profiles decay with r^{-1} in the innermost region ($r \lesssim 0.03$ pc), resembling the simulation by Ressler et al (2018). Although not shown here, the control run (started at $t = -1100$ yr) displays the same behavior at the present time. In the disk phase, the profiles deviate significantly from their quasi-steady phase shapes. The disk formation increases the density by about an order of magnitude, which extends up to ~ 0.01 pc from Sgr A*. On the contrary, the temperature profile decreases by an order of magnitude but, at the same time, becomes slightly steeper. Analyzing the disk structure at the end of the simulation, we observe that the disk has a mass of $\sim 5 \times 10^{-3} M_\odot$, with a temperature of $\sim 10^4$ K. We ran the model for an extra 1000 yr into the future and found that the disk is not destroyed, instead its mass increases at an average rate of $\sim 10^{-6} M_\odot$ yr.

Figure 5 is a Hammer projection as seen from the Sgr A* location that shows the evolution of the direction of the averaged angular momentum of the gas enclosed in a sphere of radius 0.01 pc (0.25 arcsec) in the quasi-steady (dashed blue line), and disk (solid orange line) phases. The angles Ω and i correspond to the longitude of the ascending node and inclination, respectively. The earliest time is represented with a triangle marker, while the latest with square marker. As a reference, we include the angular momentum direction of the WR

stars (black stars), as well as of the stellar clockwise disk at $\Omega = 104^\circ$ and $i = 126^\circ$ (Yelda et al. 2014). Notice that in the quasi-steady phase the angular momentum direction is highly variable due to the stochastic accretion of material coming from different stars that have a close passage from Sgr A*. However, most of the time the angular momentum direction is consistent with the stars, whose orbits are located near the clockwise disk. This is expected given that these stars have relatively slower winds (~ 600 km s $^{-1}$) and orbit closer to the black hole ($\lesssim 0.3$ pc), such that their wind angular momentum is smaller (Cuadra et al. 2008; Ressler et al 2018). In the disk phase, initially the angular momentum of the gas is aligned with the stellar disk, and more specifically with IRS 33E, but ultimately precesses around $(\Omega, i) \approx (90^\circ, 0^\circ)$. Notice that this precession could be an undesired effect due to the Cartesian grid.

4. DISCUSSION

We have shown that, if modeled for a long enough timescale ($\gtrsim 3000$ yr), the natural outcome of the evolution of the WR stellar system is a disk-like structure around Sgr A*. The crucial conditions for this to occur are the interaction between the wind of one particular star, IRS 33E, and the dense medium, together with modelling the system at least a complete orbit with such a dense medium built. Although the mass loss rate of the star is average for a WR type ($\sim 1.6 \times 10^{-5} M_\odot$ yr $^{-1}$), its wind speed is the slowest among all the stars (450 km s $^{-1}$; Martins et al. 2007). Thus, the ram pressure of its wind is weak, which forces

it to be denser at the stagnation point. As a result, the shocked material radiates most of its thermal energy almost instantaneously (see Section 4.1 in Calderón et al. 2016, for a discussion). This can be seen in the form of a dense, cold bow shock in front of the star while orbiting around Sgr A* (see panel d of Figure 2). Figure 1 shows that the pericenter and apocenter distances of the star are 0.069 pc and 0.213 pc from the SMBH, respectively. Therefore, the star oscillates between the regimes where the net mass flow to Sgr A* is ~ 0 and where the outflow dominates (see Figure 12 of Ressler et al 2018). In this scenario, the star feeds the nucleus during every pericenter passage of its ~ 2000 yr orbit (see Figure 1). However, this occurs thanks to the presence of a dense medium that interacts with the wind. In contrast, the control run does not show this behavior likely due to limited simulation time once the dense environment is established.

Nonetheless, there are a couple of caveats we have to bear in mind when interpreting this result. High-resolution simulations of idealized stellar wind collisions have shown that the dense clumps formed are neither massive nor large ($\lesssim 10^{-3} M_{\oplus}$; Calderón et al. 2019). The parameters of such models were largely motivated by the WR stars in the Galactic Center. In principle, this would suggest that the clumpy structure observed in the larger-scale simulation presented here might not be resolved, being smaller and less massive in reality. That being said, it is not straightforward to extrapolate the earlier result to our current configuration, as the mechanism creating clumps here is different. Being so, the disruption of a dense stellar wind bow shock in this environment is a promising channel for clump formation, and possibly G2-like objects (Burkert et al. 2012), unlike colliding winds (Calderón et al. 2016, 2018, 2019).

In order to check potential numerical effects on the result we ran a couple of extra tests. Firstly, we used a MinMod flux limiter, which resulted in the same observed behavior, or even better as the disk did not precess and remained aligned with the clockwise disk. Nevertheless, one of the caveats with this approach is that the winds are not spherically symmetric for reasonable computational costs. Secondly, we decreased the density

threshold of the refinement criterion, which results in a more uniform grid. The same behavior was observed but the disk formed slightly later.

Overall, the accumulation of material around Sgr A* takes place on timescales of thousands of years, which leads to an enhancement in both the mass inflow and outflow rates (see Figure 3). Despite the higher accretion, once the disk forms, Sgr A* is still in the so-called radiatively inefficient accretion flow (RIAF) regime. In this context, as the material is very hot, it can overheat and then eject a big fraction of mass and energy in the form of a strong outflow (Blandford & Begelman 1999; Begelman 2012). The disk seen in the simulation could then have produced the inferred larger luminosity for Sgr A* (Ponti et al. 2010), and/or triggered the reported outflow (Wang et al. 2013; Do et al. 2019). In that case, it is not clear whether the disk still exists or if it was destroyed by such an outflow. But the cold gas reported by Murchikova et al. (2019), if confirmed as a disk, could correspond to the one from our models. In fact, in order to match the H30 α and Br- γ observational constraints, we require an amplification factor of ~ 30 , consistent with the masing factor ~ 80 reported by Murchikova et al. (2019). However, considering the expected interaction of G2 with this disk, the density we find is an order of magnitude higher than the one derived by Gillessen et al. (2019) from the cloud slow-down.

To conclude, we speculatively propose that the stellar winds alone can be responsible for much of the phenomenology observed and/or inferred in the central arc-second during the last millenium: the variable accretion and luminosity, a cold disc, and an outflow. If so, there is no need to invoke “external” factors such as infalling gas from Sgr A West (a.k.a., the *minispiral*), a tidal disruption event and/or a supernova.

We thank the anonymous referee for useful comments and suggestions to improve this article. DC and JC acknowledge the kind hospitality of the Max Planck Institute for Extraterrestrial Physics as well as funding from the Max Planck Society through a “Partner Group” grant. We thank F. E. Bauer and J. Dexter for useful discussions and suggestions for improving this work. The authors acknowledge support from CONICYT project Basal AFB-170002. DC is supported by CONICYT-PCHA/Doctorado Nacional (2015-21151574). CMPR is supported by FONDECYT grant 3170870. Numerical simulations were run on the high-performance computing system COBRA of the Max Planck Computing and Data Facility. Data analysis was carried out making use of the PYTHON package YT (Turk et al. 2011).

REFERENCES

- Baganoff, F. K., Maeda, Y., Morris, M., et al. 2003, ApJ, 591, 891
 Begelman, M. C. 2012, MNRAS, 420, 2912
 Beloborodov, A. M., Levin, Y., Eisenhauer, F., et al. 2006, ApJ, 648, 405
 Blandford, R. D., & Begelman, M. C. 1999, MNRAS, 303, L1
 Burkert, A., Schartmann, M., Alig, C., et al. 2012, ApJ, 750, 58
 Calderón, D., Ballone, A., Cuadra, J., et al. 2016, MNRAS, 455, 4388
 Calderón, D., Cuadra, J., Schartmann, M., et al. 2018, MNRAS, 478, 3494
 Calderón, D., Cuadra, J., Schartmann, M., et al. 2019, arXiv e-prints, arXiv:1906.04181
 Crowther, P. A. 2007, ARA&A, 45, 177
 Cuadra, J., Nayakshin, S., Martins, F. 2008, MNRAS, 383, 458
 Cuadra, J., Nayakshin, S., Wang, Q. D. 2015, MNRAS, 450, 277
 Do, T., Witzel, G., Gautam, A. K., et al. 2019, ApJL, 882, L27

- Genzel, R., Eisenhauer, F., Gillessen, S. 2010, *Rev. Mod. Phys.*, 82, 3121
- Gillessen, S., Genzel, R., Fritz, T. K., et al. 2012, *Nature*, 481, 51
- Gillessen, S., Plewa, P., Eisenhauer, F., et al. 2017, *ApJ*, 837, 30
- Gillessen, S., Plewa, P. M., Widmann, F., et al. 2019, *ApJ*, 871, 126
- Gravity Collaboration, Abuter, R., Amorim, A., et al. 2018, *A&A*, 618, L10
- Fritz, T. K., Gillessen, S., Dodds-Eden, K., et al. 2010, *ApJ*, 721, 395
- Koyama, K., Maeda, Y., Sonobe, T., et al. 1996, *PASJ*, 48, 249
- Lemaster, M. N., Stone, J. M., Gardiner, T. A. 2007, *ApJ*, 662, 582
- Marrone, D. P., Moran, J. M., Zhao, J.-H., et al. 2006, *ApJ*, 640, 308
- Marrone, D. P., Moran, J. M., Zhao, J.-H., et al. 2007, *ApJL*, 654, L57
- Martins, F., Genzel, R., Hillier, D. J., Eisenhauer, F., Paumard, T., Gillessen, S., Ott, T., Trippe, S. 2007, *A&A*, 468, 233
- Muno, M. P., Baganoff, F. K., Brandt, W. N., et al. 2007, *ApJL*, 656, L69
- Murchikova, E. M., Phinney, E. S., Pancoast, A., et al. 2019, *Nature*, 570, 83
- Paumard, T., et al. 2006, *ApJ*, 643, 1011
- Ponti, G., Terrier, R., Goldwurm, A., Belanger, G., Trap, G., 2010, *ApJ*, 714, 732
- Ressler, S. M., Quataert, E., & Stone, J. M. 2018, *MNRAS*, 478, 3544
- Russell, C. M. P., Wang, Q. D., & Cuadra, J. 2017, *MNRAS*, 464, 4958
- Sunyaev, R. A., et al. 1993, *ApJ*, 407, 606
- Teyssier, R. 2002, *A&A*, 385, 337
- Toro, E. 2009, *Riemann Solvers and Numerical Methods for Fluid Dynamics: A Practical Introduction*. Springer, Berlin Heidelberg
- Turk, M. J., Smith, B. D., Oishi, J. S., et al. 2011, *ApJS*, 192, 9
- Wang, Q. D., et al. 2013, *Science*, 341, 981
- Yelda, S., Ghez, A. M., Lu, J. R., Do, T., Meyer, L., Morris, M. R., Matthews, K. 2014, *ApJ*, 783, 131